

PAPER

Directly Determining the Interface Structure and Band Offset of a Large-Lattice-Mismatched CdS/CdTe Heterostructure

Recent citations

- [Machine Learning Kinetic Energy Functional for a One-Dimensional Periodic System](#)
Hong-Bin Ren *et al*

To cite this article: Quanyin Tang *et al* 2020 *Chinese Phys. Lett.* **37** 096802

View the [article online](#) for updates and enhancements.

Directly Determining the Interface Structure and Band Offset of a Large-Lattice-Mismatched CdS/CdTe Heterostructure

Quanyin Tang(汤权银)¹, Ji-Hui Yang(杨吉辉)^{1,3}, Zhi-Pan Liu(刘智攀)², and Xin-Gao Gong(龚新高)^{1,3*}

¹Key Laboratory for Computational Physical Sciences (MOE), State Key Laboratory of Surface Physics, Department of Physics, Fudan University, Shanghai 200433, China

²Key Laboratory for Computational Physical Sciences (MOE), Shanghai Key Laboratory of Molecular Catalysis and Innovative Materials, Department of Chemistry, Fudan University, Shanghai 200433, China

³Shanghai Qi Zhi Institute, Shanghai 200232, China

(Received 2 July 2020; accepted 27 July 2020; published online 1 September 2020)

The CdS/CdTe heterojunction plays an important role in determining the energy conversion efficiency of CdTe solar cells. However, the interface structure remains unknown, due to the large lattice mismatch between CdS and CdTe, posing great challenges to achieving an understanding of its interfacial effects. By combining a neural-network-based machine-learning method and the stochastic surface walking-based global optimization method, we first train a neural network potential for CdS/Te systems with demonstrated robustness and reliability. Based on the above potential, we then use simulated annealing to obtain the optimal structure of the CdS/CdTe interface. We find that the most stable structure has the features of both bulks and disorders. Using the obtained structure, we directly calculate the band offset between CdS and CdTe by aligning the core levels in the heterostructure with those in the bulks, using one-shot first-principles calculations. Our calculated band offset is 0.55 eV, in comparison with 0.70 eV, obtained using other indirect methods. The obtained interface structure should prove useful for further study of the properties of CdTe/CdS heterostructures. Our work also presents an example which is applicable to other complex interfaces.

PACS: 68.35.-p, 71.20.Nr, 71.55.Gs

DOI: 10.1088/0256-307X/37/9/096802

Cadmium telluride (CdTe), one of the II–IV types of compound semiconductors, is a promising material for thin-film solar cells, as it has an ideal direct bandgap of about 1.45 eV, and large optical absorption coefficients. Usually, a CdTe solar cell is composed of a heterojunction of p-type CdTe and n-type CdS, which function as an absorber layer and a window layer, respectively.^[1–3] To date, CdTe solar cells based on such an architecture have achieved a record efficiency of up to 22.1%,^[4] making CdTe solar cells very competitive, due to their low cost and high efficiency.

However, there is still a great deal of room for the further improvement of CdTe solar cells, because its Shockley–Queisser efficiency limit is about 29%.^[5] Of its many efficiency-affecting factors, the interface at the heterojunction is expected to play a key role. On the one hand, the band alignment between CdTe and CdS is beneficial for carrier separations. Both theoretical calculations and experiments show that the valence band maximum (VBM) of CdTe is about 0.5–1 eV higher than that of CdS,^[6–8] which can prevent holes from running into CdS,^[9] thereby suppressing carrier recombination and improving performance. On the other hand, the large lattice mismatch between CdS and CdTe may induce

disorders, stacking faults and grain boundaries, at which deep-level defects may segregate and act as carrier recombination centers.^[10–12] In addition, S–Te inter-diffusion, and the formation of a CdS_xTe_{1–x} alloy^[13–15] can have more complex effects, such as altering the material bandgap and band alignments near the interface,^[16–19] thereby reducing the lattice mismatch at the CdTe/CdS interface, and altering the interfacial states and recombination centers.^[20]

Owing to the critical role played by this interface, it is extremely important to understand the interfacial effects occurring in CdTe solar cells, which are, as yet, unclear. Theoretically, this understanding faces two predominant challenges: firstly, the atomic structure at the interface is not known. Current studies mainly construct small heterostructure supercells of CdTe and CdS, using their average lattice constants. Obviously, this approach is far from reflecting reality, because a large strain exists on both sides. Secondly, if the real lattice constants were to be used, a very large supercell would be required to simulate the heterostructure. Structural relaxation of such a large supercell cannot usually be performed using first-principles calculations based on density functional theory (DFT),^[21,22] and one has to rely on classical methods based on empirical potentials. However,

Supported by the National Natural Science Foundation of China (Grant No. 11974078), the Fudan Start-up Funding (Grant No. JIH1512034), and the Shanghai Sailing Program (Grant No. 19YF1403100).

*Corresponding authors. Email: xggong@fudan.edu.cn

© 2020 Chinese Physical Society and IOP Publishing Ltd

their accuracy and reliability cannot be guaranteed, since, as far as we know, reliable empirical potentials are still lacking for such systems.

To overcome the above challenges, and theoretically understand the interfacial effects in CdTe solar cells, in this paper, we first train a global neural network (NN) potential for CdTe systems, combining the neural-network-based machine-learning method and the stochastic surface walking (SSW)^[23,24] based global optimization method.^[25,26] Our convergence test shows that the NN potential can be used to effectively predict the properties, not only of bulks, but also of systems with point defects, thus demonstrating that the NN's potential is robust and adaptive for complex atomic environments. Based on our trained NN potential, the optimal structure is obtained by simulating the annealing^[27–30] process of the CdS/CdTe interface. We find that the most stable structure has features of both bulks and disorders. Using the obtained heterostructure, we then directly calculate the band offset between CdS and CdTe by aligning the core levels^[31] in the heterostructure and those in the bulks, using one-shot first-principles calculations. Our calculation result is about 0.55 eV as compared with 0.70 eV, obtained using other indirect methods.

Self-Learning Procedures. Global high-dimensional NN potentials are numerical functions of a large number of structural parameters, also known as structural descriptors.^[32–34] Due to a lack of analytical forms, the common routine for obtaining NN potentials is via machine learning methods. During the machine learning procedure, training data sets, consisting of a series of structures as inputs, and the corresponding total energies as outputs, should be provided. Using the training datasets, the potential energy surface (PES) in the structural phase space is constructed, and the global NN potential can then be obtained. To ensure the reliability of the NN potentials, the training dataset, the PES, and global NN potential should be consistent with one another.

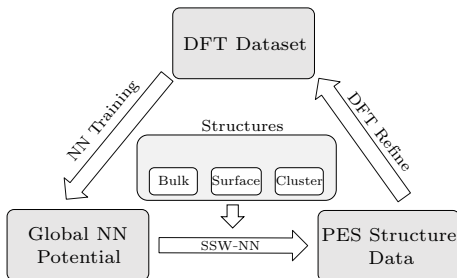


Fig. 1. Self-learning procedure for global NN potential. Firstly, an initial dataset is generated, using first-principles calculations. The dataset is then trained to obtain global NN potentials. Next, the global NN potential energy surface is explored and sampled by the SSW method, and an additional dataset is generated and added to the initial dataset. Finally, a new cycle of self-learning begins, refining the global NN potential.

In this work, we adopt the self-learning procedure proposed previously by one of the authors^[26] to obtain NN potentials for our systems. As shown in Fig. 1, the first step is to generate an initial dataset from first-principles calculations based on density functional theory. The second step is to train a rough NN potential, using the neural-network-based machine-learning method from the current-existing dataset. The potential energy surface is then explored and sampled by the SSW method^[23,24] to generate further structures, calculated using DFT, to obtain the total energies. The additional dataset is then added into the initial dataset. Finally, a new cycle of self-learning starts to refine the global NN potential. During the machine learning process, we first construct the input layer using power-type structural descriptors (PTSDs) to distinguish different structures on PES.^[25,26,35] The PTSDs are expressed as follows:

$$f_c(r_{ij}) = \begin{cases} 0.5 \tanh^3 \left[1 - \frac{r_{ij}}{r_c} \right], & r_{ij} \leq r_c, \\ 0, & r_{ij} > r_c, \end{cases} \quad (1)$$

$$R^n(r_{ij}) = r_{ij}^n f_c(r_{ij}), \quad (2)$$

$$S_i^1 = \sum_{j \neq i} R^n(r_{ij}), \quad (3)$$

$$S_i^2 = \left[\sum_{m=-L}^L \left| \sum_{j \neq i} R^n(r_{ij}) Y_{Lm}(r_{ij}) \right|^2 \right]^{1/2}, \quad (4)$$

$$S_i^3 = 2^{1-\zeta} \sum_{j,k \neq i} (1 + \lambda \cos \theta_{ijk})^\zeta R^n(r_{ij}) R^m(r_{ik}) R^p(r_{jk}), \quad (5)$$

$$S_i^4 = 2^{1-\zeta} \sum_{j,k \neq i} (1 + \lambda \cos \theta_{ijk})^\zeta \cdot R^n(r_{ij}) \cdot R^m(r_{ik}), \quad (6)$$

$$S_i^5 = \left[\sum_{m=-L}^L \left| \sum_{j,k \neq i} R^n(r_{ij}) R^m(r_{ik}) R^p(r_{jk}) \cdot [Y_{Lm}(r_{ij}) + Y_{Lm}(r_{ik})]^2 \right|^2 \right]^{1/2}, \quad (7)$$

$$S_i^6 = 2^{1-\zeta} \sum_{j,k,l \neq i} (1 + \lambda \cos \delta_{ijkl})^\zeta R^n(r_{ij}) R^m(r_{ik}) R^p(r_{il}), \quad (8)$$

where r_{ij} is the distance between atoms i and j , and θ_{ijk} is the angle centered at i atom, with j and k being neighbors. Here, f_c is the cutoff function, which decays to zero beyond r_c . S_i^1 and S_i^2 are two-body functions, S_i^3 , S_i^4 , and S_i^5 are three-body functions, and S_i^6 is a four-body function, with superscripts 1, 2... 6 denoting different structures. With regard to the hidden layers, we use two layers with 50 parameters for each layer.

Computational Details. DFT calculations are performed using the Vienna *ab initio* simulation package (VASP).^[36] The electron-ion interaction is treated by the projector augmented wave (PAW)^[37] type pseudopotential, and the kinetic energy cutoff of the plane

wave is set to 450 eV. For the exchange-correlation functional, the generalized gradient approximation (GGA) of Perdew–Burke–Ernzerhof (PBE)^[38] is used. Large numbers of k -point samples, with an automatic k -point generation scheme at 25 \AA^{-1} , are used to ensure the convergence of the calculated results. The NN potential is trained and refined via the self-learning procedures implemented in the Large-scale Atomistic Simulation with neural network potential (LASP).^[39] All the parameters are maintained during the NN potential training process and the convergence test.

The interface structure is optimized, using the simulated annealing method, through molecular dynamic simulations, in which an isobaric-isothermal ensemble is adopted for each temperature. The initial structure is heated from 300 K to a high temperature, then cooled down to 300 K. At each temperature, the total simulation time is 10 ps, with a time step of 1 fs.

Convergence Test of the Global NN Potential. In order to create the NN potential for CdSTe, we adopted a large set of structural descriptors, containing 205 PTSDs, i.e., 55 S^1 , 46 S^2 , 24 S^3 , 54 S^4 , 22 S^5 , and 4 S^6 . After careful training and refining, we obtained a high-quality NN potential, with root-mean-square error values between NN and DFT results of 8.065 meV per atom, 0.135 eV/Å, and 0.673 GPa for energy, force and stress, respectively.

To examine the accuracy of the PES, we compare the results of NN potentials with DFT calculations for the representative structures of bulk crystals and systems with point defects, as listed in Tables 1 and 2. For bulks, we can see that the energy difference ΔE between the NN potential and DFT results are very small, demonstrating the high degree of accuracy of the NN potential. It is even able to provide the correct energy orders for the zinc-blende (ZB) and wurtzite (WZ) structures of CdS and CdTe.^[40,41] For example, the results from our NN potentials show that the energy of ZB-CdS is 0.3 meV/atom higher than that of WZ-CdS, in agreement with the DFT results, which show that ZB-CdS has an energy of 1.1 meV/atom higher than that of WZ-CdS. Similarly, the energy of ZB-CdTe is 4.7 meV/atom or 7.3 meV/atom lower than WZ-CdTe from the results of NN potentials or DFT calculations, respectively. For systems with defects, we consider various point defects in CdS and CdTe. As shown in Table 2, the difference in terms of the total energies of defective supercells ΔE , and the difference in terms of defect formation energies ΔE_f are in a reasonable range. All the above convergence tests indicate that the NN potential created here demonstrates great accuracy and robustness in relation to investigating CdSTe systems.

Table 1. NN potential verification for bulk systems, including Cd, S, Te, CdS, and CdTe. The total energies E are calculated using both the NN potential and DFT for structures relaxed by the NN potential. Lattice constants are also listed in the table. The results demonstrate the high degree of accuracy of the NN potential.

		Cd	S	Te	CdS (ZB)	CdS (WZ)	CdTe (ZB)	CdTe (WZ)
NN	a (Å)	3.096	8.568	4.544	5.940	4.198	6.637	4.690
	c (Å)	5.540	15.00	5.901		6.856		7.659
	E (eV/Atom)	-0.8995	-4.1357	-3.1340	-3.1604	-3.1607	-2.4882	-2.4835
DFT	a (Å)	3.147	9.248	4.512	5.936	4.203	6.623	4.682
	c (Å)	5.155	13.642	5.960		6.835		7.663
	E (eV/Atom)	-0.8613	-4.1237	-3.1398	-3.1602	-3.1613	-2.4898	-2.4825
	ΔE (meV/Atom)	-38.2	-12.0	5.8	-0.2	0.6	1.6	1.0

Table 2. NN potential verification for CdS and CdTe with point defects. The total energy E and its differences ΔE in terms of the NN potential and DFT results are the order of 1 meV/atom, and the differences of defect formation energies ΔE_f are within 1%. All energies are expressed in units of eV.

Defect type	E (NN)	E (DFT)	ΔE	E_f (NN)	E_f (DFT)	ΔE_f
CdS +V _{Cd}	-399.9370	-399.7771	-0.1599	3.7327	3.7413	-0.0085
CdS +V _S	-397.8033	-397.8223	0.0190	2.6302	2.4336	0.1967
CdS +Te _S	-403.0955	-403.0020	-0.0934	0.4721	0.3936	0.0785
CdTe +V _{Cd}	-156.0004	-155.9798	-0.0206	2.3420	2.5102	-0.1681
CdTe +V _{Te}	-153.0542	-152.9634	-0.0908	3.0537	3.2480	-0.1943
CdTe +S _{Te}	-160.4013	-160.4478	0.0465	-0.1577	-0.1127	-0.0450

Atomic Structure of CdS/CdTe Interface. Having created a well-trained global NN potential for CdSTe, our next step is to obtain stable structures for the CdS/CdTe interface. First of all, we need to construct an initial structural model for the CdS/CdTe interface. As the lattice constants of WZ-CdS and ZB-CdTe optimized by NN potential are 4.19 Å and

6.63 Å, respectively, with a large lattice mismatch of about 11% between the [111] surface of CdTe and the [0001] surface of CdS [see Fig. 2(a)], we use 9×9 [0001] of CdS to match 8×8 [111] of CdTe [see Fig. 2(b)] with a suitable bond length at their interface. The entire interface model, as illustrated in Fig. 2(c), comprises 1740 atoms, with two layers of CdS and three layers of

CdTe. Having obtained the initial structure, we then perform structural relaxation at zero temperature; the resulting relaxed structure is shown in Fig. 2(d).

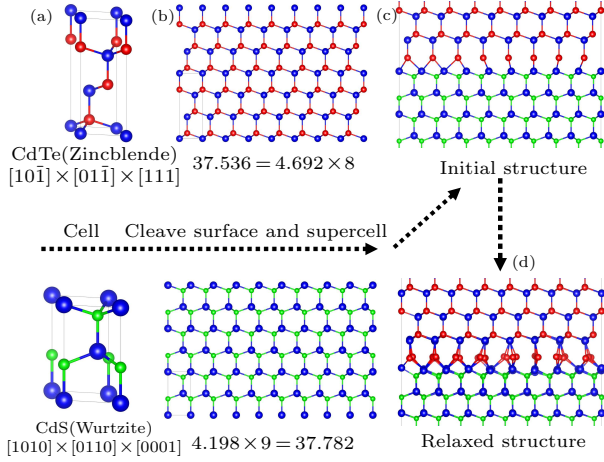


Fig. 2. Flowchart showing the construction of the initial interface structure of the CdS/CdTe heterojunction. (a) Cells of CdTe and CdS along selected directions. (b) Supercells of cleaved surfaces of CdS and CdTe. (c) Initial interface structure. (d) Relaxed structure of (c). The blue, red and green balls represent Cd, Te, and S atoms, respectively.

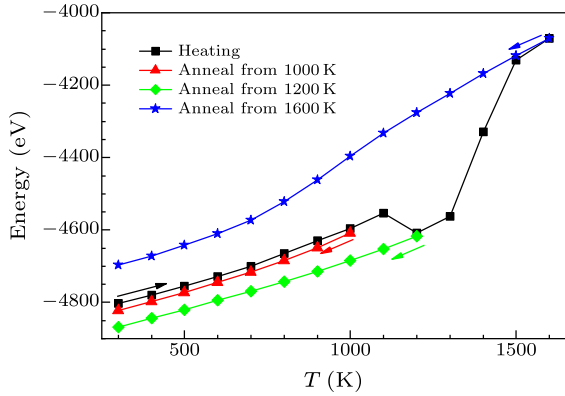


Fig. 3. Average energies of samples taken from molecular dynamic simulations as functions of temperatures during the heating and annealing process. The black line indicates the heating simulation curve, and the red, green and blue lines show annealing curves for 1000 K, 1200 K and 1600 K, respectively. The “bowl” shape of the heating curve, and the non-coincident of the annealing process curves indicate that the initial structure is not the most stable structure; the most stable structure is that obtained by annealing at 1200 K.

Based on the above relaxed structure, we then perform molecular dynamic annealing simulations using our NN potential to obtain stable interface structures. We first increase the simulation temperature from 300 K to a high temperature and then decrease the temperature back to 300 K. As shown in Fig. 3(a), the black line indicates the heating process, and the structures are then annealed at 1000 K (red line), 1200 K (green line) and 1600 K (blue line), respectively. As can be seen, different annealing temperatures result in different structures. If annealing the sample at a lower temperature, i.e., 1000 K, we obtain a structure with

a similar energy to that of the initial structure. If annealing the sample from 1200 K to 300 K, we achieve a more stable structure, which is physically reasonable, and will be discussed in detail below. In contrast, if annealing from 1600 K to 300 K at the same annealing rate, a more unstable structure is obtained. The reasons for this can be explained as follows: if the annealing temperature is too low, the structure at the annealing temperature will be just a relaxed version of the initial structure, which cannot cross the barrier on the PES to achieve a more stable local minimum. If the annealing temperature is too high, the sample will become liquid, and thus can easily be trapped at a local minimum with a high entropic energy at the selected annealing speed. When the temperature drops, the sample gets stuck, and the structure becomes metastable due to the large reduction in entropic energy. Only if the annealing temperature is between 1200 K and 1300 K can the structure overcome the barrier on the PES to reach a more stable minimum, which can still be maintained after the temperature drops.

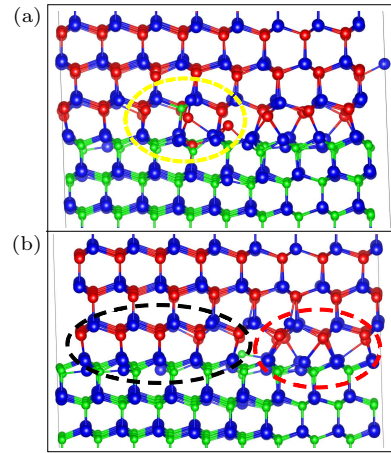


Fig. 4. (a) Interface structure obtained by annealing from 1200 K to 300 K. Note the appearance of S-Te inter-diffusion, indicated by the yellow dashed line. (b) Interface structure without inter-diffusion. Note that this is composed of two regions: bulks and dislocation-like disorders, as indicated by the black and red dashed lines. The energy of structure (a) is about 0.6 eV higher than that of structure (b), which implies that inter-diffusion may appear at finite temperatures.

The more stable structure obtained by annealing the sample from 1200 K to 300 K is shown in Fig. 4(a). We find that S and Te can diffuse into CdTe and CdS, respectively, making the interface a kind of alloy of CdSTe, in agreement with the experimental findings that CdSTe alloys will form at high temperatures.^[13–15]

To eliminate the alloy effect and focus only on the pure interface structure at this stage, we replace the diffused S and Te atoms with Te and S, respectively. Following this substitution, we obtain a new structure, as shown in Fig. 4(b). Our first-principles calculations show that, at zero temperature, this new

structure is more energetically favorable, with a total energy of about 0.6 eV lower than that with S and Te inter-diffusion. The reason why the unalloyed structure is not found in the annealing simulation is that the alloyed interface structure is more stable at relatively high temperatures, such as 1200 K, due to the entropic contribution. At room temperature, the unalloyed structure is still more stable, and therefore we will use the unalloyed structure in the discussions which follow.

In order to verify the stability of the obtained structure in Fig. 4(b), we repeat the heating and annealing simulation. Our simulation results are shown in Fig. 5, where the lines have the same meanings as those in Fig. 3. In contrast to Fig. 3, however, the heating curve monotonically increases with increasing temperature, indicating that there are no structural changes during the heating process. Similarly to the first annealing process, an unstable structure is obtained if annealing from 1600 K to 300 K, since the structure at 1600 K is already liquid-like. As anticipated, if we anneal the sample from any temperature below 1300 K, we can always obtain the initial structure, indicating that the initial structure is a stable structure of the interface.

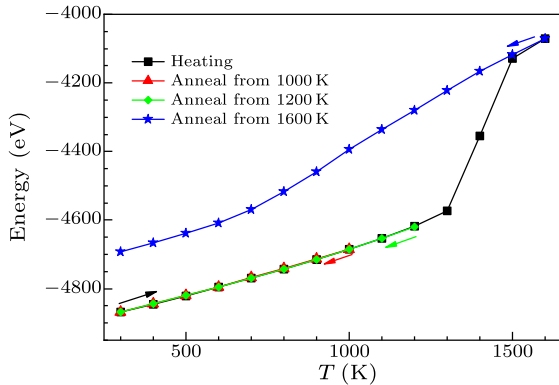


Fig. 5. Average energies of samples from the molecular dynamic simulations, versus temperatures during the second simulated annealing process. The coincidence of the heating and annealing processes shows that the initial structure of the simulation is stable. The black, red, green and blue lines indicate the heating simulation, annealing from 1000 K, 1200 K and 1600 K, respectively.

As shown in Fig. 4, the stable interface structure is clearly significantly different from the initial artificially-built structure. In the artificially built structure, the atoms near the interface are uniformly arranged. In contrast, the most stable structure in Fig. 4(b) is composed of two regions, bulks and dislocation-like disorders, as indicated by black and red dash blanks, respectively. Such arrangements are anticipated to reduce the stress induced by the large lattice mismatch, thereby stabilizing the interface. In fact, the coordination numbers of atoms at the interface are also changed. As is well-known, the Cd, S and Te atoms in perfect crystals such as CdS or

CdTe are tetra-coordinated. Consequently, the numbers of non-tetra-coordinated atoms can be used to describe the relative stability of the structure. In the stable interface structure shown in Fig. 4(b), there are 10 three-coordinated Cd and 4 three-coordinated Te atoms, which form the core of the dislocation-like disorder in the interface. In contrast, there are 42 three-coordinated Te and 61 five-coordinated Cd atoms in the initial structure [see Fig. 2(d)]. Compared to the initial interface structure, the numbers of non-tetra-coordinated atoms and dangling bonds are reduced in the stable structure.

To further demonstrate the stability of this interface structure, we calculate its interface energies, which are defined as follows:

$$\gamma = \frac{\Delta E}{2S} = \frac{E - \sum_i n_i E_i}{2S}, \quad (9)$$

where ΔE is the interface formation energy, E_i denotes the component energy, and S is the area of the interface. We find that the interface energy of the most stable interface is about $0.0087 \text{ eV}/\text{\AA}^2$, only about one third of the interface energy of the initial structure, which is $0.028 \text{ eV}/\text{\AA}^2$.

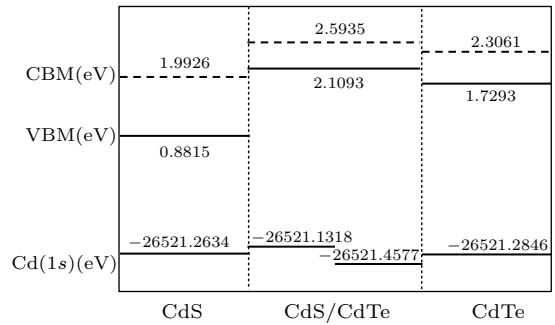


Fig. 6. Band offset of CdS and CdTe. By aligning the 1s levels of Cd far away from the CdTe/CdS interface to those in CdTe and CdS bulks, respectively, we find that the VBM of CdTe is 0.55 eV higher than that of CdS.

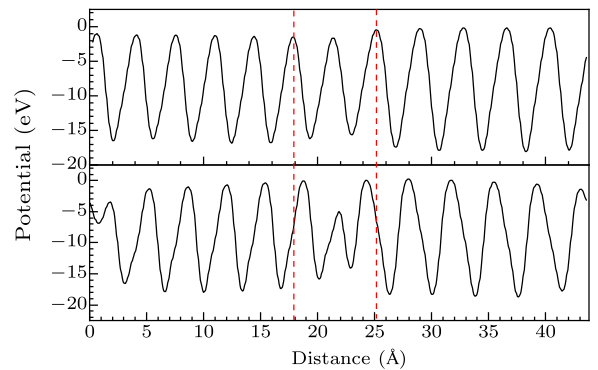


Fig. 7. Local potential of the CdS/CdTe interface. The upper section shows the stable interface [see Fig. 4(b)], and the lower section shows the initial hand-built model with relaxation [see Fig. 2(d)]. The red dashed lines show the interface, and the stable interface smooths the sharp potential fluctuations.

Band Offset and Local Potential. Having obtained a structural model of the CdTe/CdS heterostructure,

we can now directly perform first-principles calculations to study the interface effect on electronic properties, i.e., the band offset between CdTe and CdS, as well as the local potential at the interface. Following the conventional routine, as shown in Fig. 6 we align the 1s levels of Cd far away from the CdTe/CdS interface to those in CdTe and CdS bulks, respectively, to obtain the relative positions of the VBM of CdTe and CdS. Our calculation shows that the VBM of CdTe is 0.55 eV higher than that of CdS, in comparison with the theoretical value, using the three-step method^[42] of 0.70 eV, and the experimental value of 0.50–1.00 eV.^[6–8,40,43–45] To show the importance of choosing the most stable interface structure for determining the band alignments at the heterostructure, we compare the band offset results obtained from the two structures in Figs. 2(d) and 4(b). We find that the artificially built structure with relaxations only gives a band offset value of 0.20 eV. Such a large discrepancy can be understood on the basis of the local potentials at the interface. As shown in Fig. 7, the most stable interface significantly reduces the potential difference across the CdS/CdTe heterojunction, compared to the artificially built version.

In conclusion, we have trained a robust and reliable neural network potential for CdS/CdTe systems by combining the neural-network-based machine-learning method and the stochastic surface walking-based global optimization method. Based on this potential, we have obtained a stable interface structure of the CdS/CdTe heterostructure, which is partially dislocation-like. Using the obtained heterostructure, we have directly calculated the band offset between CdS and CdTe, and our result is about 0.55 eV, comparable with the 0.70 eV result obtained using other indirect methods. This work increases our understanding of the physics of CdTe/CdS heterostructures in the CdTe solar cell, as well as the process of exploring complicated interface structures.

Computation in this work was performed in the Supercomputer Center, Fudan University.

References

- [1] Britt J and Ferekides C 1993 *Appl. Phys. Lett.* **62** 2851
- [2] Wu X Z 2004 *Sol. Energy Mater.* **77** 803
- [3] Il'chuk G, Kusnez V, Rud V Y, Rud Y V, Shapoval P Y and Petrus R Y 2010 *Semiconductors* **44** 318
- [4] Green M A, Dunlop E D, Levi D H, Hohl-Ebinger J, Yoshita M and Ho-Baillie A W Y 2020 *Prog. Photovoltaics* **28** 3
- [5] Shockley W and Queisser H J 1961 *J. Appl. Phys.* **32** 510
- [6] Wei S H, Zhang S B and Zunger A 2000 *J. Appl. Phys.* **87** 1304
- [7] Dharmadasa I M, Samantilleke A P, Chauré N B and Young J 2002 *Semicond. Sci. Technol.* **17** 1238
- [8] Boieriu P, Sporken R and Sivananthan S 2002 *J. Vac. Sci. & Technol. B* **20** 1777
- [9] Minemoto T, Matsui T, Takakura H, Hamakawa Y, Negami T, Hashimoto Y, Uenoyama T and Kitagawa M 2001 *Sol. Energy Mater. Sol. Cells* **67** 83
- [10] Loginov Y Y, Durose K, AlAllak H M, Galloway S A, Oktik S, Brinkman A W, Richter H and Bonnet D 1996 *J. Cryst. Growth* **161** 159
- [11] Li C, Poplawsky J, Yan Y F and Pennycook S J 2017 *Mater. Sci. Semicond. Process.* **65** 64
- [12] Smith D J, Lu J, Aoki T, McCartney M R and Zhang Y H 2017 *J. Mater. Res.* **32** 921
- [13] McCandless B E, Moulton L V and Birkmire R W 1997 *Prog. Photovoltaics* **5** 249
- [14] McCandless B E, Engelmann M G and Birkmire R W 2001 *J. Appl. Phys.* **89** 988
- [15] Wu X, Asher S, Levi D H, King D E, Yan Y, Gessert T A and Sheldon P 2001 *J. Appl. Phys.* **89** 4564
- [16] Ohata K, Saraie J and Tanaka T 1973 *Jpn. J. Appl. Phys.* **12** 1641
- [17] Pal R, Dutta J, Chaudhuri S and Pal A K 1993 *J. Phys. D* **26** 704
- [18] Klein A 2015 *J. Phys.: Condens. Matter* **27** 134201
- [19] Lane D W 2006 *Sol. Energy Mater. Sol. Cells* **90** 1169
- [20] Oman D M, Dugan K M, Killian J L, Ceekala V, Ferekides C S and Morel D L 1995 *Appl. Phys. Lett.* **67** 1896
- [21] Hohenberg P and Kohn W 1964 *Phys. Rev. B* **136** B864
- [22] Kohn W and Sham L J 1965 *Phys. Rev.* **140** A1133
- [23] Shang C and Liu Z P 2013 *J. Chem. Theory Comput.* **9** 1838
- [24] Shang C, Zhang X J and Liu Z P 2014 *Phys. Chem. Chem. Phys.* **16** 17845
- [25] Huang S D, Shang C, Zhang X J and Liu Z P 2017 *Chem. Sci.* **8** 6327
- [26] Ma S C, Shang C and Liu Z P 2019 *J. Chem. Phys.* **151** 050901
- [27] Lewis N S 2007 *Science* **315** 798
- [28] Alder B J and Wainwright T E 1959 *J. Chem. Phys.* **31** 459
- [29] Gibson J B, Goland A N, Milgram M and Vineyard G H 1960 *Phys. Rev.* **120** 1229
- [30] Rahman A 1964 *Phys. Rev.* **136** A405
- [31] Wei S H and Zunger A 1998 *Appl. Phys. Lett.* **72** 2011
- [32] Behler J and Parrinello M 2007 *Phys. Rev. Lett.* **98** 146401
- [33] Artrith N, Morawietz T and Behler J 2011 *Phys. Rev. B* **83** 153101
- [34] Behler J 2014 *J. Phys.: Condens. Matter* **26** 183001
- [35] Huang S D, Shang C, Kang P L and Liu Z P 2018 *Chem. Sci.* **9** 8644
- [36] Kresse G and Furthmüller J 1996 *Comput. Mater. Sci.* **6** 15
- [37] Kresse G and Joubert D 1999 *Phys. Rev. B* **59** 1758
- [38] Perdew J P, Burke K and Ernzerhof M 1996 *Phys. Rev. Lett.* **77** 3865
- [39] Huang S D, Shang C, Kang P L, Zhang X J and Liu Z P 2019 *WIREs Comput. Mol. Sci.* **9** e1415
- [40] Wei S H and Zhang S B 2000 *Phys. Rev. B* **62** 6944
- [41] Wright K and Gale J D 2004 *Phys. Rev. B* **70** 035211
- [42] Lang L, Zhang Y Y, Xu P, Chen S Y, Xiang H J and Gong X G 2015 *Phys. Rev. B* **92** 075102
- [43] Niles D W and Höchst H 1990 *Phys. Rev. B* **41** 12710
- [44] Fritzsche J, Schulmeyer T, Kraft D, Thissen A, Klein A and Jaegermann W 2002 *Appl. Phys. Lett.* **81** 2297
- [45] Gu H J, Zhang Y Y, Chen S Y, Xiang H J and Gong X G 2018 *Phys. Rev. B* **97** 235308